



Article

Confining Fluorescent Probes in Nanochannels to Construct Reusable Nanosensors for Ion Current and Fluorescence Dual Gating

Dan Zhang¹, Chunfei Wang¹, Changfeng Wu² and Xuanjun Zhang^{1,*}

¹ MOE Frontiers Science Center for Precision Oncology, Faculty of Health Sciences, University of Macau, Macau 999078, China; yb97663@um.edu.mo (D.Z.); chunfeiwang@um.edu.mo (C.W.)

² Department of Biomedical Engineering, Southern University of Science and Technology, Shenzhen 518055, China; wucf@sustech.edu.cn

* Correspondence: xuanjunzhang@um.edu.mo

Abstract: Here, we confined fluorescent probes to solid nanochannels to construct nanosensors, which not only significantly improved the reusability of the molecular probes, but also achieved ion current and fluorescence dual gating for more reliable detection. The combination of optical and electrical modalities can provide comprehensive spatiotemporal information that can be used to elucidate the sensing mechanism within the nanochannel. As a proof-of-concept experiment, fluorescein isothiocyanate (FITC)–hydrazine (N₂H₄) was selected to modify nanochannels for the effective detection of Hg²⁺. Based on spirolactam opening tactics, the system synergistically alters the surface charge and fluorescence intensity in response to Hg²⁺, establishing a dual open state of current and fluorescence. The newly prepared nanosensor exhibited a fast response (<1 min), high sensitivity, and selectivity towards Hg²⁺. Importantly, the nanodevice could be recovered by simple N₂H₄ treatment. Such sensing behavior could be used to implement optoelectronic dual-output XOR logical gates under the management of Hg²⁺ and N₂H₄. This strategy is anticipated to find broad applications in other nanochannel-based systems for various sensing applications used for monitoring of pollutants, food additives, and biomolecules.

Keywords: nanochannel sensor; dual gating; ion current; fluorescence; Hg(II); reusable



Citation: Zhang, D.; Wang, C.; Wu, C.; Zhang, X. Confining Fluorescent Probes in Nanochannels to Construct Reusable Nanosensors for Ion Current and Fluorescence Dual Gating. *Nanomaterials* **2022**, *12*, 1468. <https://doi.org/10.3390/nano12091468>

Academic Editor: Antonios Kelarakis

Received: 2 March 2022

Accepted: 24 April 2022

Published: 26 April 2022

Publisher's Note: MDPI stays neutral with regard to jurisdictional claims in published maps and institutional affiliations.



Copyright: © 2022 by the authors. Licensee MDPI, Basel, Switzerland. This article is an open access article distributed under the terms and conditions of the Creative Commons Attribution (CC BY) license (<https://creativecommons.org/licenses/by/4.0/>).

1. Introduction

Inspired by biological protein channels, biomimetic solid-state nanochannels with ordered porous structures have received a large amount of research interest in the biochemical sensing field in recent decades [1–6]. Owing to their strong mechanical rigidity and flexible tunability in terms of geometry and surface modification [7–13], these nanochannels can be used as a promising skeleton to confine different types of probes, including small molecules and biomolecules (e.g., DNA, RNA, and proteins) [5,13–15]. Upon proper immobilization with the designed probes, targets can interact specifically with these functional molecules to change the nanochannels' properties, such as their surface charge, wettability, and/or effective aperture [3–5,14–17]. Owing to the confining effect within nanochannels, these changes eventually trigger a highly sensitive response to transmembrane ion currents [18,19]. Additionally, the sensitive single electronic readout from picoampere to nanoampere is susceptible to nonspecific adsorption, obstruction of orifices, and/or different operation and equipment, increasing the likelihood of false-positive errors [20,21]. The lack of spatial visualization further blurs the actual response process inside the channel and erodes our ability to judge the corresponding reaction mechanism [22,23]. Monitoring fluorescence in nanochannels provides a direct and convenient way to assess spatial information. Although nanochannels can be lightened by attaching fluorescent dyes to nanochannel surfaces [24–26], this fluorophore is not involved in the sensing process,

and does not reflect the reactivity of target analytes. Therefore, confining fluorescent probes into a nanochannel system can effectively fuse the complementary strengths of small-molecule fluorescent probes and nanochannels to achieve the current–fluorescence dual-signal monitoring of the analytes and improve the reusability of expensive probes. Additionally, benefiting from the unique confinement effect of the special microenvironment of nanochannels, the probe-functionalized sensor allows for the detection of lower concentrations and increases the detection sensitivity.

Mercury ions (Hg^{2+}) are among the most toxic metal contaminants, and are widely distributed in solution matrices [27]. Mercury, in any form, can pose a serious and permanent threat to cell architecture function and human health by damaging the DNA, brain, kidneys, and digestive and central neurological systems—even in trace amounts [27–29]. The World Health Organization (WHO) and the US Environmental Protection Agency (EPA) have set the maximum allowable limits of Hg^{2+} in drinking water to 30 and 10 nM, respectively [30,31]. To date, abundant mercury-indicating techniques in water samples have been reported, typically including liquid molecule fluorescence sensors and solid-state nanochannel platforms. Among them, the fluorescence probe for Hg^{2+} based on a fluorescein derivative promises fruitful applications due to its fast response time and visual monitoring. Its chemistry has also been well documented [32]. When spiro lactam formation (cyclization) between fluorescein and N_2H_4 occurs, the emission intensity of fluorescein hydrazide is very low. After binding to Hg^{2+} ions, Hg^{2+} can induce the spiro ring to open and form fluorescein, resulting in a dramatic increase in the green fluorescence. However, the liquid phase fluorescent assay has limited ability for cyclic detection due to their easy photobleaching, difficulty to separate, and poor recoverability [33,34]. In addition, all reported nanochannel sensors towards Hg^{2+} are based on the specific interaction between Hg^{2+} and thymine (T)-rich DNA probes to form stable T- Hg^{2+} -T complexes [25,26,35,36]. This conformational shift triggers an effective pore size change to control the transmembrane current. However, the formation of a double-stranded rigid structure requires a reaction time of several hours. Its reaction mechanism in the channel also lacks an intuitive verification method, such as fluorescence signals [24,36,37]. Accordingly, it is imperative to exploit fast, reusable, and reliable sensors for the analysis of Hg^{2+} in aqueous samples. The transfer of effective spiro-ring switch events into solid nanochannels may easily enable the reuse of probes and dual-mode monitoring of current and fluorescence.

Herein, as a prototype example, we confined spiro fluorescent probes in solid nanochannels to construct a reusable Hg^{2+} nanosensor with dual gating of ionic current and fluorescence (Figure 1). After achieving stepwise attachment of fluorescein isothiocyanate (FITC) and hydrazine (N_2H_4) to the channels, the FITC- N_2H_4 probe in the closed spiro lactam form showed a positive charge and weak fluorescence. At this point, the nanochannels presented a dual-closed gating status of current and fluorescence. Upon detection of Hg^{2+} , the probe would isomerize to a ring-opening form, leading to a negatively charged state and fluorescence enhancement at the same time. Therefore, the original optoelectronic dual-closed gating was converted into dual-open gating. Importantly, the probe can be readily recycled to the ring-closed form by reacting with N_2H_4 . This feature endows the nanochannel sensor with reversible switching via the alternative stimulation of Hg^{2+} and N_2H_4 . It is therefore used to support the development of current and fluorescence dual-output XOR logical gates. Our nanochannel platform allows for mutual verification of the detection results obtained from the dual electro-optical modes, effectively improving the accuracy and reliability of the detection.

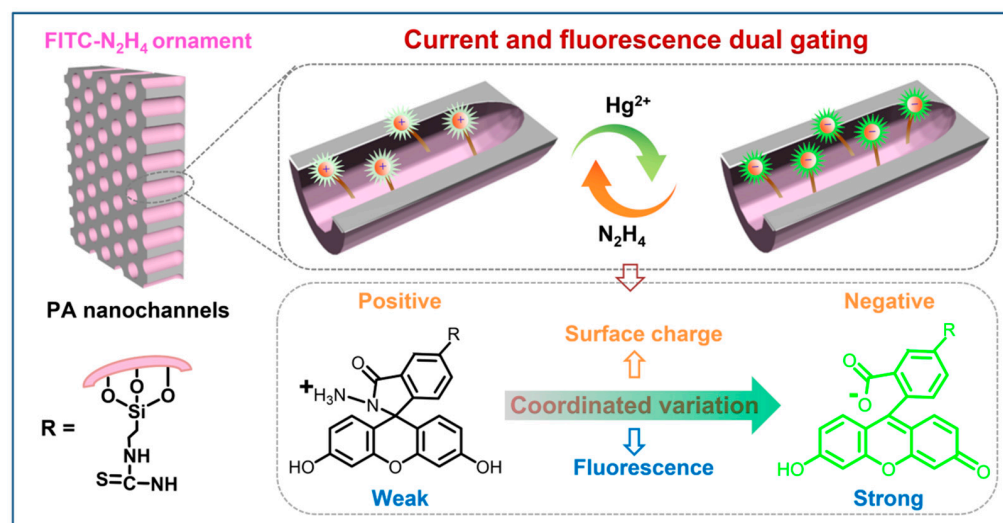


Figure 1. Schematic of the reusable Hg^{2+} -responsive nanochannel sensor for current and fluorescence dual gating. The detector is based on FITC- N_2H_4 -modified alumina nanochannels. The FITC- N_2H_4 probe is reversible upon alternative treatment with Hg^{2+} and N_2H_4 .

2. Materials and Methods

2.1. Materials

Perchloric acid (HClO_4), phosphoric acid, chromium trioxide, and potassium chloride were purchased from Beijing Chemical Works (Beijing, China). Oxalic acid ($\text{H}_2\text{C}_2\text{O}_4$) was purchased from Aladdin (Shanghai Aladdin Biochemical Technology Co., Ltd, Shanghai, China). Fluorescein, hydrazine hydrate ($\text{N}_2\text{H}_4 \cdot \text{H}_2\text{O}$), hydrogen peroxide (H_2O_2), potassium hydroxide (KOH), hydrochloric acid (HCl), mercury(II) nitrate dihydrate ($\text{Hg}(\text{NO}_3)_2 \cdot 2\text{H}_2\text{O}$), and other metal salts were purchased from Sigma-Aldrich (Sigma-Aldrich, Inc., St. Louis, MO, USA). (3-Aminopropyl) triethoxysilane (APTES) and fluorescein isothiocyanate (FITC) were purchased from Dieckmann (Dieckmann Technology Development Co., Ltd., Shenzhen, China). Silver wire, platinum wire, stainless steel sheets, and aluminum foil (99.999% pure) were purchased from Trillion Metals Co., Ltd (Beijing, China). All chemicals were supplied by commercial distributors and used without further purification.

2.2. Characterization

The surface morphologies of the nanotube-shaped alumina nanochannels at the base and tip sides, as well as their cross-sections, were characterized using an FEI Quanta FEG 250 environmental scanning electron microscope (SEM). Chemical analysis of the composition and elements of Al_2O_3 nanochannels upon the modification of each step was conducted using an ESCALAB 250Xi XPS (Thermo Fisher Scientific, Waltham, MA, USA). Water contact angles (CAs) were measured using an OCA40 contact angle system (DataPhysics, Filderstadt, Germany). Fluorescence spectroscopy and confocal images were performed using a HORIBA FluoroLog-3 Modular Spectrofluorometer (Horiba Instruments, Acal BFi, Eindhoven, The Netherlands) and a Carl Zeiss LSM710 confocal microscope (Carl Zeiss Pty Ltd., Oberkochen, Germany), respectively. The excitation wavelength was set to 488 nm.

After the attachment of FITC on the nanochannel surface, fluorescence spectroscopy (XPS) analysis revealed a new S2p peak at 165 eV, which was due to the sulfur element of FITC. The decrease in the CA value indicated a more hydrophilic surface. The ionic current in the $I-V$ analysis increased in the reverse direction, indicating a negative surface charge generated by the FITC. In fluorescence spectroscopy, the distinct peak at 518 nm is the characteristic emission peak of FITC. In laser confocal imaging, green fluorescence was observed in the cross-section of the nanochannel, directly indicating that the FITC had successfully attached to the interior of the nanochannel. However, after being treated with

hydrazine, the content of nitrogen elements increased, which was attributed to the cyclization reaction of FITC with hydrazine. The increase in CA indicated a decrease in surface hydrophilicity. In the I - V analysis, the ionic current decreased and the direction reversed again, indicating the positive surface charge from N_2H_4 . In fluorescence spectroscopy, the characteristic fluorescence peak from FITC at 518 nm was significantly decreased. In laser confocal imaging, the original green fluorescence was not observed. These results suggested that the further conjugation of N_2H_4 with FITC in the nanochannels triggered spiro lactam formation. In a word, based on XPS, CA, I - V curves, fluorescence spectroscopy, and confocal images, we can clearly demonstrate the successful modification of FITC and N_2H_4 on the surface of the nanochannel.

2.3. Preparation of the Nanotube-Shaped Alumina Nanochannels

The nanotube-shaped alumina nanochannels were prepared via two-step anodization combined with etching of the aluminum substrate and the barrier layer [38,39]. Firstly, Al foil (99.999% pure) was cleaned with acetone, ethanol, and Milli-Q water (18.2 M Ω) successively. Then, the resulting Al foil was used as the anode to conduct electropolishing in a mixed solution of $HClO_4$ and ethanol (1:4 in volume ratio) at 5 °C under a voltage of 17 V for 7 min to achieve a mirror-finished surface, while a graphite plate was used as the cathode. Subsequently, the first anodization was carried out in a 0.3 M oxalic acid solution at 5 °C for 2 h. However, the obtained disordered porous oxide layer needed to be peeled off the Al substrate in a mixing solution containing 6 wt% phosphoric acid and 3.5 wt% chromic acid at 90 °C for 2 h. Then, the residual Al substrate with hemispherical concaves was re-anodized for 6 h under the same conditions as the first anodization to grow highly ordered Al_2O_3 porous arrays. To expose the barrier oxide layer against the porous Al_2O_3 arrays, sodium hydroxide and saturated copper dichloride solution were continuously used to etch away the bottom of the Al substrate. Finally, the accurate pore-opening procedure of the barrier layer in 6 wt% H_3PO_4 was the key to regulating the transmembrane ion transport properties. The adjustment for pore size was closely dependent on the remaining time. Morphologies at the barrier layer side after the etching were observed via SEM.

2.4. Sequential Immobilization of APTES, FITC, and N_2H_4 on the Nanochannels

The as-prepared nanotube-shaped Al_2O_3 nanochannels were firstly boiled in hydrogen peroxide for 1 h to introduce more hydroxylate groups onto the inner surface of the nanochannels. The resulting nanochannels were immersed in an ethanol solution of APTES (16 wt%) for 1 h to enrich the pore surface with amino groups. Such free amino groups were used for covalently immobilizing FITC through the formation of thiourea bonds overnight. With that, the FITC-functionalized nanochannels carrying carboxylic groups further reacted with N_2H_4 (25 mM) overnight in ethanol solution. All of the membranes were washed with ethanol solution and deoxygenated Milli-Q water (18.2 M Ω) before I - V measurement.

2.5. Ionic Current Measurements

The ionic current and rectification characteristics of nanochannels under various states of modification were characterized by investigating transmembrane I - V curves at varied scanning voltages from -2 to $+2$ V, which were provided by a Keithley 6487 picoammeter (Keithley Instruments, Cleveland, OH, USA). Aqueous potassium chloride solution at 1 mM was chosen as the electrolyte. The nanochannel membrane was mounted between two chambers of the electrochemical cell, in each of which one Ag/AgCl electrode was vertically installed to produce the transmembrane potential driving electrolytes across the nanochannels. The base side of the alumina nanochannels was determined to provide the positive potential, while the tip side was found to provide the negative potential. All of the tests were conducted at room temperature. The response measurement was conducted on the PA channel after being treated with Hg^{2+} for 15 min, unless otherwise specified.

3. Results and Discussion

3.1. Characterization of the Nanochannels

The porous alumina nanochannels were fabricated via a two-step anodization method combined with an etching procedure of the aluminum substrate and the barrier layer, as reported in [38,39]. The entire nanochannel exhibited an asymmetric geometric skeleton similar to that of a nanotube. As investigated by scanning electron microscopy (SEM), the thickness of the resultant alumina nanochannels was estimated at 25 μm (Figure 2a). The diameter of the intermediate parallel channels was approximately 35 nm (Figure 2b), which was equivalent to the aperture at the opening base side (Figure 2c). Conversely, at the tip side, a close-packed semispherical hexagon on the barrier layer could be observed (Figure S1a). This impeded the smooth transport of ions across the membrane. Therefore, to increase the membrane permeability while maintaining asymmetric nanotube traits, the pore-opening procedure of the barrier layer was precisely controlled by adjusting the chemical etching time (Figure 2d and Figure S1b,c). The results show that the diameter of the tip side increased appreciably with increasing etching time. As a result, the structure of the nanochannel membrane was transformed from asymmetric to symmetric. A typical SEM observation (Figure 2d) of the bottom surface showed the appearance of tiny, subnanometer-wide cracks after 10 min of etching, which could provide a confined transmission path for ions. In this case, maximizing the asymmetric morphology (Figure 2e) would lead to optimal ion transport behavior, including ionic conduction and ionic rectification.

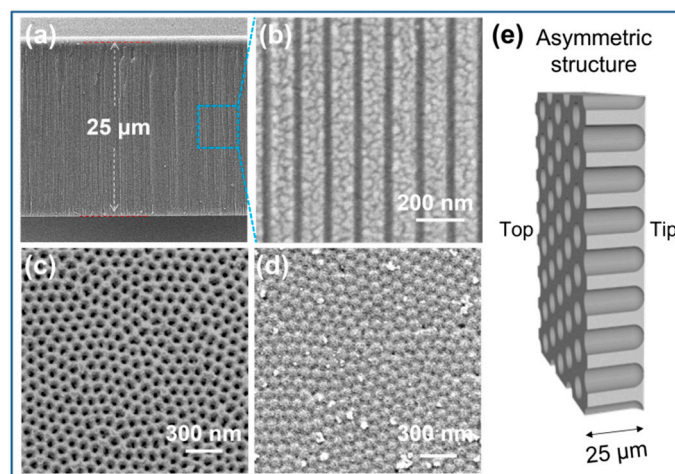


Figure 2. SEM images from (a,b) the cross-sectional view of the alumina nanochannel at low and high magnifications, respectively, and from (c,d) the opening base and tip sides of the Al_2O_3 barrier layer, respectively. (e) As a whole, the nanochannels present an asymmetric structure.

3.2. Construction of the Functionalized Nanochannel Sensor

Given the ring-opening recognition behavior of spiro lactam towards Hg^{2+} , the FITC- N_2H_4 probes were selected to be covalently grafted onto the inner surface of the alumina nanochannels by stepwise modifications (Figure 3a). (3-Aminopropyl) triethoxysilane (APTES), as a bifunctional molecular glue, can effectively conjugate the FITC to the Al_2O_3 channels. The triethoxysilane group can be bonded to the Al_2O_3 surface via the Al-O-Si bond, while the amino group can conjugate with fluorescein isothiocyanate via thiourea [40]. In the next step, the Hg^{2+} -response moiety, -CONNH₂, was formed in situ by simple N_2H_4 treatment. The final probe-functionalized alumina (PA) nanochannels were thoroughly washed with ethanol to remove any unconjugated free molecules. Throughout the process, from the Al_2O_3 channel to the APTES channel, as well as the FITC channel and the PA channel, the surface charge was transformed by positively charged hydroxyl groups ($-\text{OH}_2^+$), positively charged amino groups ($-\text{NH}_3^+$), negatively charged carboxyl groups

($-\text{COO}^-$), and positively charged $-\text{NH}_3^+$. Meanwhile, the probes grafted to the channels showed fluorescence quenching due to the spirolactam closing.

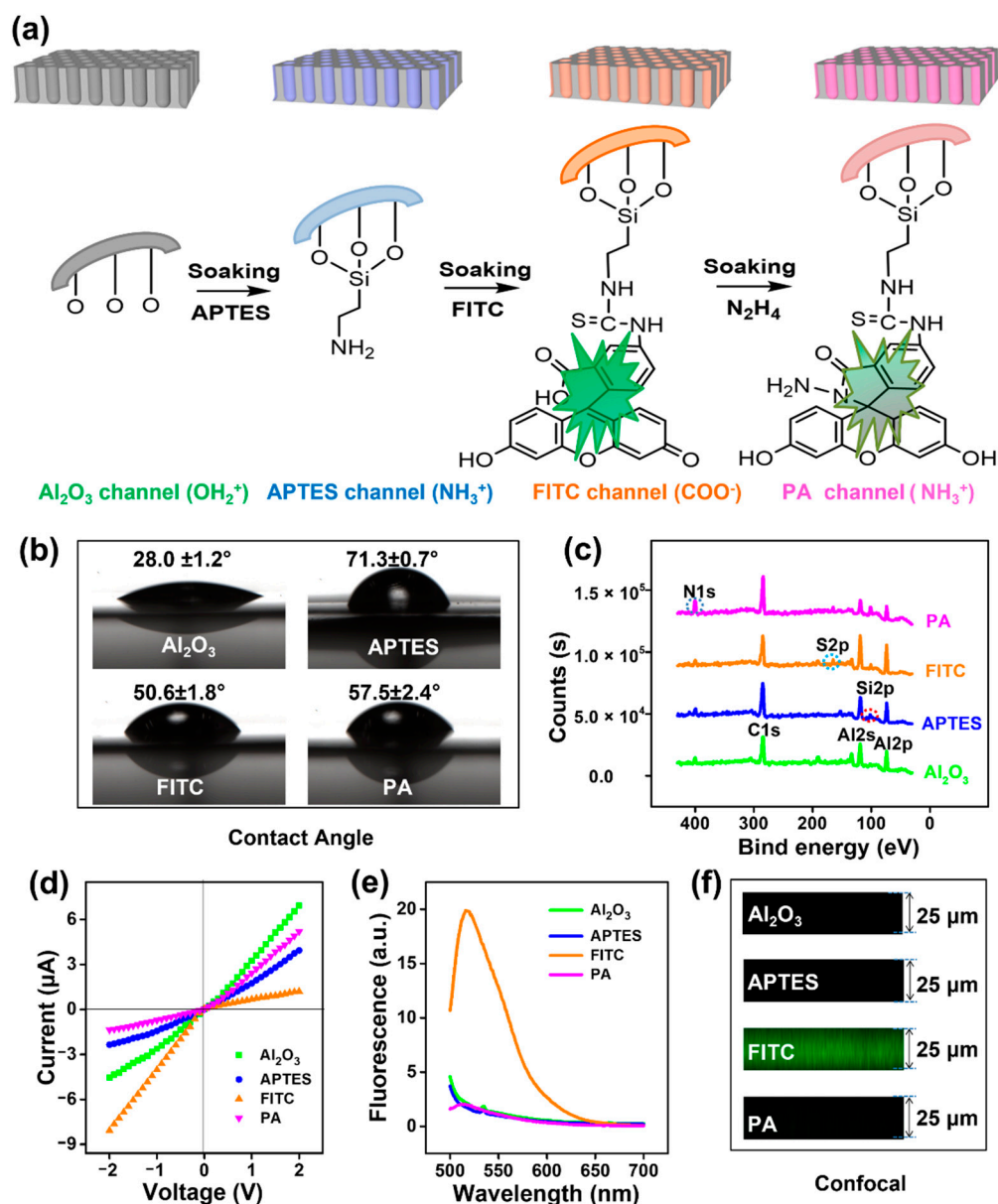


Figure 3. Characterization of the nanochannel modification process: (a) The construction evolution for Hg^{2+} -gated nanochannels from Al_2O_3 to APTES, FITC, and probe-modified alumina (PA) nanochannels by APTES, FITC, and N_2H_4 soaking treatment, in sequence. In this process, the surface charge and fluorescence characteristics of the nanochannels were changed; the characterizations for these channels via (b) wettability, (c) elemental composition studied by XPS, (d) I - V curves, (e) fluorescence spectra, and (f) confocal imaging.

Successful stepwise modifications were confirmed by contact angle (CA) measurement and X-ray photoelectron spectroscopy (XPS) (Figure 3b,c). As expected, the attachment of APTES and FITC on the nanochannel surface resulted in a new Si2p peak at 103 eV and an S2p peak at 165 eV [41,42]. After being treated with hydrazine, the content of nitrogen elements in the FITC-modified nanochannels increased. This was due to the cyclization reaction of FITC with hydrazine. The modification was further characterized by typical transmembrane current-voltage (I - V) responses, which were recorded in a two-compartment electrochemical reservoir filled with 1 mM electrolytic KCl solutions

(Figure S2). The change in wettability had an effect on ion conduction. The change in the polarity of the surface charge resulted in a reversal of the direction of current rectification. As shown in Figure 3d, before modification, the channel surface was positively charged ($-\text{OH}_2^+$) in neutral electrolytes because the isoelectric point (IEP) of the terminal hydroxyl groups on alumina was approximately 8.7 [43]. In this case, more chloride would be attracted into asymmetric nanoconfined Al_2O_3 spaces. These chloride anions preferred to flow from the tip to the base side at a positive voltage, thus bringing about an ionic rectification behavior—higher currents at positive voltages than at negative voltages. Compared with other channels, the highest current conduction at +2 V for Al_2O_3 should be attributed to its superhydrophilic nature, with CAs of approximately 28° . After modification by APTES, the current rectification direction of the alumina nanochannels did not change, as the inner surface rich in amine groups was shown to be positively charged. However, ion conduction of the APTES channel was significantly reduced due to its enhanced hydrophobicity, which hindered ion transport across the membrane to some extent [40]. The introduction of FITC chromophores on the channel triggered an immediate reversal of the rectification characteristics and augmented the current conduction at -2 V. This was attributed to the deprotonation of $-\text{COOH}$ groups from FITC, which formed a negatively charged hydrophilic surface. Finally, the electronegative carboxyl groups were replaced by amino groups through subsequent N_2H_4 treatment, and the current rectification direction was reversed again. Accordingly, the rectification properties provided more intuitive evidence for the successful modification and the transition in surface charge (Figure S3).

In addition, fluorescence spectroscopy (Figure 3e) and laser confocal imaging (Figure 3f) in view of spatial information were employed to track the modification progress of probe molecules. FITC, as a fluorescein derivative, has strong green fluorescence. The excitation wavelength was 488 nm. As a result, the green fluorescence peak at 518 nm appeared after FITC was attached to the surface of the nanochannel, while the original AAO and APTES channels had no fluorescence peaks (Figure 3e). By cross-sectional confocal imaging, obvious green fluorescence could be observed from the FITC nanochannels (Figure 3f). These intuitive fluorescence signals clearly indicated that FITC was successfully attached to the inner surface of the nanochannel, whereas the further conjugation of N_2H_4 with FITC triggered spiro lactam formation, resulting in significant declines in the fluorescence intensity [44]. As shown in Figure 3e,f, the emission peak and green fluorescence intensity were dramatically reduced after N_2H_4 treatment. The changes in spatial fluorescence indicate that cyclization of FITC in the nanochannels occurs readily with N_2H_4 .

3.3. Current and Fluorescence Dual Gating and Renewability of the Nanosensor

We investigated whether the probe molecules confined in nanochannels could trigger fluorescence and current dual gating. As shown in Figure 4a, a rectification behavior was observed in asymmetric PA nanochannels, with a lower conductance at -2 V. This is because in the confined space of protonated NH_3^+ , Cl^- was selectively transported through the channel from its tip side. However, under stimulation with Hg^{2+} ($10 \mu\text{M}$), the ionic conductance at -2 V immediately increased to $-6.94 \mu\text{A}$ from $-1.36 \mu\text{A}$, and a reversal of the rectification characteristics occurred. The wettability of the channel membrane also increased with the ionic conductance (the CA decreased from $57.5 \pm 2.4^\circ$ to $51.0 \pm 1.3^\circ$). This might have been due to the specific catalytic reaction between the Hg^{2+} and the CONNH_2 moiety of the fluorescent probe, which can trigger the ring opening of spiro lactam and the charge transformation from positive (NH_3^+) to negative (COO^-). In this case, more K^+ cations could be attracted into the channels, resulting in an inversion of current rectification and enhancement in current conduction at -2 V. Meanwhile, the recovery of the FITC component on the channel surface also intrinsically turned on fluorescence, as revealed by both fluorescence spectra and fluorescence confocal imaging (Figure 4b). The fluorescence change trend in response to Hg^{2+} in the channel system was consistent with that of the free fluorescein- N_2H_4 molecule (Figure S4) in the solution system (Figure S5). The detailed response mechanism is shown in Figure S6. As reported, the Hg^{2+} can first

chelate N and O on the hydrazone group of the probe to form a fluorescein–N₂H₄–Hg²⁺ complex. Then, the metal–ligand complex undergoes hydrolysis of the amide bond to assist the ring opening, resulting in the formation of fluorescein [42,45,46]. The entire process triggers a conformational transformation from fluorescein spirolactam to ring-opening fluorescein. This ring-opening phenomenon was also supported by corresponding hydrogen nuclear magnetic resonance spectrum (¹H NMR) analysis (Figure S7). In short, after Hg²⁺ treatment, the closed-ring FITC–N₂H₄ probe in the liquid system was converted into an open-ring FITC component with enhanced fluorescence. When the probes were introduced into the solid nanochannels, the Hg²⁺-induced ring-opening behavior not only resulted in the enhancement of the fluorescence signal, but also caused an increase in ionic current due to the reversal of the surface charge from NH₃⁺ to COO[−]. That is, the nanochannel provides an ideal vehicle for this fluorescent probe, enabling simultaneous conversion of current and fluorescence signals. The photoelectric double-check strongly manifested the ring-opening mechanism rather than the nonspecific adsorption of targets. Importantly, the nanosensor device had excellent stability. As shown in Figure S8a,b, the responsiveness of the nanosensor to Hg²⁺ (both current and fluorescence) did not deteriorate even after a year of placement.

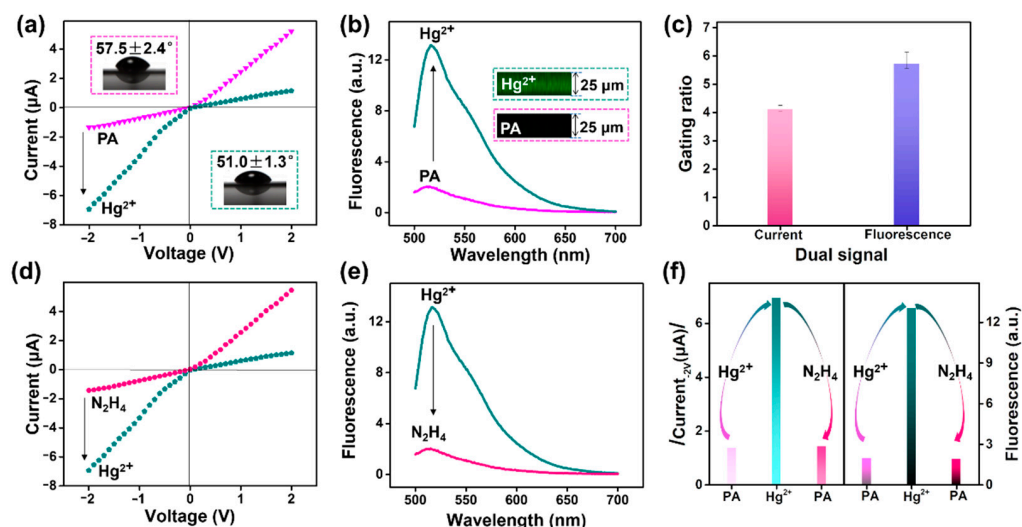


Figure 4. Current and fluorescence response of PA nanochannels to Hg²⁺ and N₂H₄: (a) *I*–*V* curves of PA nanochannels upon the treatment with 10 μM Hg²⁺; the insets represent corresponding wettability change by contact angles (CAs). (b) Fluorescence response of PA nanochannels upon the treatment with 10 μM Hg²⁺; the insets represent corresponding fluorescence images by laser scanning confocal microscopy (LSCM). (c) Hg²⁺-activated gating ratio of the current signal and fluorescence signal of the PA nanochannels. (d) *I*–*V* curves of Hg²⁺ channels upon the N₂H₄ treatment. (e) Fluorescence response of Hg²⁺ channels upon the N₂H₄ treatment. (f) Corresponding change contrast of current (absolute value at −1 V) and fluorescence upon continuous stimulation of Hg²⁺ and N₂H₄.

Gating ratios as an expression of current and fluorescence responses to Hg²⁺ were presented to discuss the performance of the nanosensor. Here, the ionic current gating ratio is defined as $((I - I_0)/I_0, -2 \text{ V})$, where *I* and *I*₀ are ionic currents at −2 V in the presence and absence of Hg²⁺, respectively. The fluorescence gating ratio is defined as $((F - F_0)/F_0, 518 \text{ nm})$, where *F*₀ and *F* are the fluorescence intensity at 518 nm before and after Hg²⁺ stimulation, respectively. Notably, the current and fluorescence gating ratios shown here were 4.1 and 5.7, respectively (Figure 4c). Accordingly, synergistic current and fluorescence gating devices were successfully built. Importantly, the ion current (Figure 4d) and fluorescence signal (Figure 4e) reversibly returned to a lower value after the reaction with N₂H₄. The combined results demonstrated that both current and fluorescence first increased after Hg²⁺ detection, and then decreased to their original values after N₂H₄

treatment (Figure 4f). In other words, the PA nanochannel sensor could be restored to its initial state under the alternating treatment with Hg^{2+} and N_2H_4 .

Based on the recovery scenarios (Figure 5a), the reusability and stability of the nanosensor were investigated by monitoring both current traces at -2 V and fluorescence intensity at 518 nm upon multiple alternating treatments with Hg^{2+} and N_2H_4 (Figure 5b) [44]. Even after five cycles, neither the current nor the fluorescence showed signs of faltering. Such robustness greatly improved the practicability of the nanosensor. Using the principle of the PA nanochannels (Figure 5a), the system was further exploited to realize two XOR logical gates by successively bringing in Hg^{2+} and N_2H_4 . This demonstrates the operational availability of the nanochannel system for current and fluorescence dual gating with reliable sensing. We considered the additions of Hg^{2+} and N_2H_4 as two input signals, and their presence and absence as “1” and “0”, respectively. For the current output, we assigned “low conduction at -2 V” as “0” and “high conductance at -2 V” as “1”. Similarly, for the fluorescence output at 518 nm, we assigned “weak fluorescence” as “0” and “strong fluorescence” as “1”. The truth table and corresponding logic scheme (Figure 5c,d) revealed that these logic operations were in accordance with a two-input and two-output excluded OR (XOR) gate (Figure 5e) [47–49]. Without (0,0) or with (1,1), and the simultaneous addition of Hg^{2+} and N_2H_4 , the surface composition of the PA channel remained as the hydrazine component. Thus, both the current and the fluorescence stayed at their low levels, producing the “0,0” dual-output signal. This suggests that the PA system is reversible for Hg^{2+} sensing. In contrast, the introduction of Hg^{2+} (1,0) alone led to the ring opening and exposure of the FITC component. In this case, ionic current at -2 V and fluorescence were significantly enhanced, featuring the “1,1” photoelectric dual output. The dual XOR logic gates in the Hg^{2+} sensor allow for higher reliability than single logic does. In a word, solid-phase attachment of fluorescent probes to the nanochannels not only offers the advantage of optical-electric bivariate detection, but also makes the sensor readily reusable. Compared to previous liquid-phase fluorescent probes or DNA-based nanochannel sensors, our nanochannel platform allows for reuse of the fluorescent probe, and also provides dual-output gates for current and fluorescence [25,32]. These features endow the monitoring system with practicality and reliability.

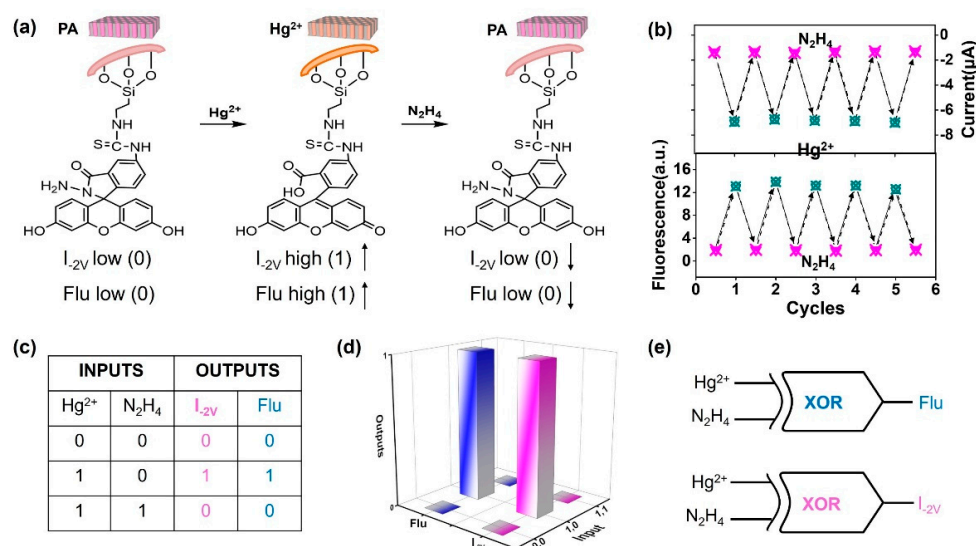


Figure 5. Recyclability of PA nanochannels and dual-output XOR gates: (a) Schematic diagram of PA nanochannels for Hg^{2+} sensing and the subsequent reversible recovery by in situ N_2H_4 treatment. (b) Current at -2 V (upper) and fluorescence (lower) cycles upon alternative stimulation of Hg^{2+} and N_2H_4 , indicating Hg^{2+} -response stability and recyclability of the PA nanochannel system. (c) Truth tables. (d) Corresponding logic functions scheme. (e) Dual-output XOR gates of the PA nanochannel system, obtained by continuously adding the Hg^{2+} and N_2H_4 as dual inputs.

3.4. Evaluation of Response Performance for Hg^{2+}

The high selectivity, sensitivity, and fast response of the nanochannel platform are desirable in effective analysis. I - V features were adopted to assess these important performance factors. To investigate the selectivity to Hg^{2+} , the nanosensor was treated with miscellaneous kinds of components (10 μM), including metal ions (Hg^{2+} , Fe^{2+} , Fe^{3+} , Pb^{2+} , Ni^{2+} , Zn^{2+} , Mn^{2+} , K^+ , Mg^{2+} , Cd^{2+} , Cu^{2+} , Ca^{2+} , Co^{2+} , and Cr^{3+}) and H_2O_2 as well as HClO . As observed in Figure 6a, the ion current at -2 V increased from -1.36 μA to -7.06 μA only after activation by Hg^{2+} . After treatment with other metal ions and reactive oxygen species, the ionic current remained unchanged. Thus, the PA system showed a higher current-gating ratio (4.2) under Hg^{2+} stimulation than the other analytes (Figure 6b). In contrast, there were no significant current and fluorescence changes in the Al_2O_3 , APTES, and FITC channels after 10 μM Hg^{2+} treatment (Figure S9a–c). It is exciting that the PA nanosensors still exhibited a high current response to Hg^{2+} in the dye-doped matrix, such as solution samples containing diversified dyes (Figure S10a) or fluorescent trackers for cell studies (Figure S10b). As long as there was no Hg^{2+} stimulation, fluorescent dyes—either alone or in combination—did not cause a change in the PA channel current. Instead, once 10 μM Hg^{2+} was introduced into this system doped with dyes, current variation in the magnitude and direction of the PA channels could be observed immediately. These merits are expected to enable this nanosystem to monitor Hg^{2+} in complicated environments, such as the printing and dyeing industries.

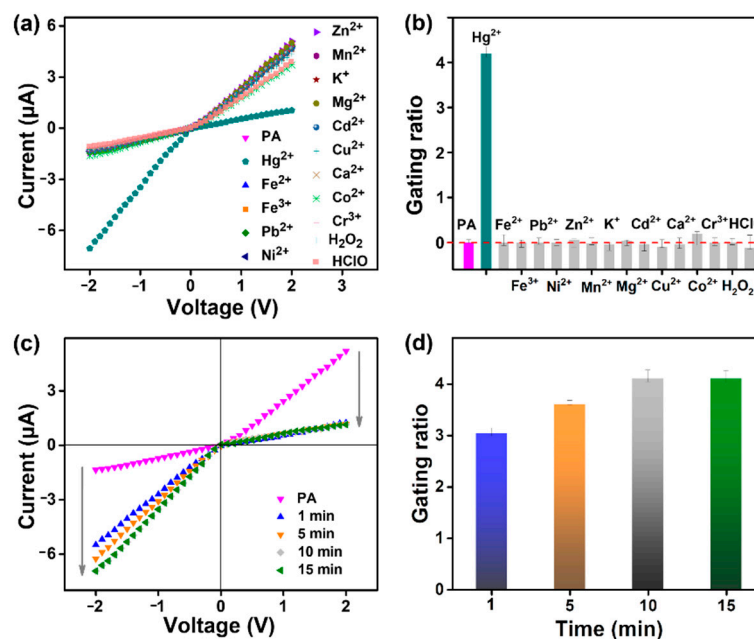


Figure 6. Selectivity and response time of the PA nanochannels to Hg^{2+} detection: (a) I - V curve performance in different analytes, and (b) the corresponding gating ratios for different analytes. (c) I - V curve performance with response time, and (d) the corresponding gating ratio.

In addition, the scanning I - V curves were investigated based on incremental response time. As shown in Figure 6c, the PA nanochannels' ionic current at -2 V was ≈ -1.36 μA . When 10 μM Hg^{2+} was applied, the current significantly increased to -5.49 μA within 1 min, and leveled off at -6.93 μA over 10 min. Even when the response was extended to 15 min, the ionic current did not increase further. Reversal of the current direction was attributed to a rapid mutation in surface charge from positive to negative. After the addition of Hg^{2+} for 1 min, the gating ratio immediately changed to 3.0, and the gate switched from the OFF to the ON state. Then, the ratio slightly increased to 3.6 at 5 min, and eventually stabilized at 4.1 over 10–15 min to reach the complete ON state (Figure 6d). Clearly, the probe-functionalized nanosystem was endowed with a fast response to Hg^{2+} .

Such molecular ring opening is faster than the formation of T-Hg²⁺-T in the DNA-based nanochannels [36].

Finally, the *I*-*V* curve response was investigated under a wide range of Hg²⁺ concentrations (Figure 7a). As the Hg²⁺ concentration increased from 1 nM to 100 μM, the ionic current at −2 V gradually rose. This suggests that the current gate switched from the OFF state to the ON state (Figure 7b). Meanwhile, the fluorescence versus Hg²⁺ concentration could also be monitored via fluorescence spectroscopy (Figure S11a) and confocal imaging (Figure S11b). As the Hg²⁺ concentrations increased, the fluorescence gating switched from the OFF state to the ON state (Figure S11c). Importantly, the plot of current versus the logarithm of the Hg²⁺ concentration (Log C, C = 1 nM–10 mM) showed a good linear correlation. As shown in Figure 7c, the typical calibration curve was $Y = -1.188 X - 5.535$ ($R^2 = 0.995$; Y and X represent the ionic current and Log C, respectively). On the grounds of a classical 3 SD/L method, where SD is the standard deviation of the blank and L is the slope of the calibration curve [5], the detection limit of this nanochannel system was estimated to be 0.23 nM. The corresponding rectifying ratio calculated in Figure 7d describes the response characteristics during Hg²⁺ recognition more intuitively. The rectifying ratio showed less variation, in the range of 10^{−9}–10^{−8} M Hg²⁺. However, when the concentration increased to 10^{−7} M, the rectifier suddenly increased to greater than 1, implying an inversion of the surface charge polarity. As the concentration of Hg²⁺ rose from 10^{−7} to 10^{−4} M, the rectifying ratio continued to increase due to the efficient ring-opening reaction producing increasing amounts of -COOH. On the whole, the newly developed nanochannel sensor had good performance in the quantitative analysis of Hg²⁺. Additionally, the designed sensing platform was successfully used for the determination of Hg²⁺ in lab wastewater (Figure S12), demonstrating its applicability in the analysis of real water samples.

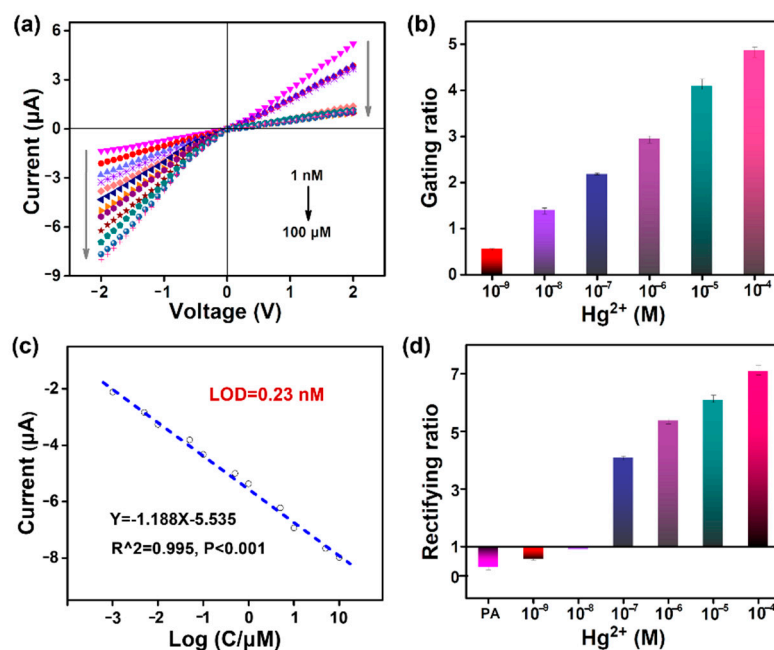


Figure 7. Sensitivity of the PA nanochannels to Hg²⁺ detection: (a) *I*-*V* curve response performance of the PA nanochannels with Hg²⁺ concentration; (b) the corresponding gating ratio, (c) detection sensitivity, and (d) rectifying ratio.

4. Conclusions

To conclude, we developed a general strategy for confining fluorescent probes in nanochannels to construct a reusable nanosensor with the dual gating of fluorescence and current. This union of temporal and spatial management allows for the mutual validation of specific recognition processes, thereby enhancing the detection reliability. In this fabrication, the FITC-N₂H₄ fluorescent probes were immobilized in the inner surface of the channel.

Upon Hg^{2+} activation, current and fluorescence synchronously switched from the OFF state to the ON state as the result of the smooth cooperative effort of surface charge reversal and fluorescence intensity enhancement by Hg^{2+} -catalyzed spiro-ring opening. In turn, the nanodevice could be restored in situ to the closed state by simple N_2H_4 treatment. Under alternating stimulation with Hg^{2+} and N_2H_4 , the nanosensor was found to exhibit excellent reversibility and stability, which can be exploited to support current and fluorescence dual-output XOR logical gates. Moreover, this Hg^{2+} -gating system exhibited a fast response within 1 min, a good sensitivity with a detection limit of 0.23 nM, and a high selectivity even in a dye-doped matrix. Overall, this strategy for confining fluorescent probes to nanochannels is versatile, and paves the way for the creation of a reusable and reliable photoelectric sensor.

Supplementary Materials: The following supporting information can be downloaded at: <https://www.mdpi.com/article/10.3390/nano12091468/s1>, Figure S1: SEM images of the tip side from an alumina barrier layer at different chemical etching times; Figure S2: Schematic representation of the experimental setup for the *I-V* measurements; Figure S3: Ionic-current-rectifying ratio characteristics of the bare Al_2O_3 , APTES, FITC, and PA nanochannels; Figure S4: The synthesis of spiro-form fluorescein hydrazide by the reaction of fluorescein with hydrazine hydrate; Figure S5: Liquid-phase fluorescence detection; Figure S6: Schematic representation of a possible mechanistic pathway of the catalytic reaction of Hg^{2+} on the non-fluorescent fluorescein- N_2H_4 probe to form highly fluorescent fluorescein; Figure S7: The ^1H NMR spectra of the fluorescein- N_2H_4 probe in the absence and presence of Hg^{2+} ; Figure S8: Current and fluorescence response to Hg^{2+} of PA nanochannels after being kept out of the light for months; Figure S9: *I-V* properties of the Al_2O_3 , APTES, and FITC nanochannels before and after Hg^{2+} stimulation; Figure S10: *I-V* curve response performance of PA nanochannels for indicating Hg^{2+} in a complex matrix containing diversified chromophore dyes or cell-tracking dyes; Figure S11: Fluorescence spectra, confocal imaging, and corresponding fluorescence gating ratios of the PA nanochannel system obtained in the presence of different concentrations of Hg^{2+} ; Figure S12: The applicability of the PA nanochannel system for the determination of Hg^{2+} in real-life samples.

Author Contributions: Conceptualization, X.Z. and C.W. (Changfeng Wu); methodology, D.Z. and C.W. (Chunfei Wang); validation, C.W. (Chunfei Wang); formal analysis, D.Z. and X.Z.; writing—original draft preparation, D.Z.; writing—review and editing, X.Z. and C.W. (Changfeng Wu); project administration, X.Z.; funding acquisition, D.Z. All authors have read and agreed to the published version of the manuscript.

Funding: This research was funded by the Science and Technology Development Fund, Macau SAR (File number 0085/2020/A2, 0114/2019/A2); the Natural Science Foundation of Guangdong Province, grant number 2022A1515010616; the Shenzhen Science and Technology Innovation Commission, grant number JCYJ20170307110157501; and the Research Grant of University of Macau, grant number MYRG2020-00130-FHS.

Institutional Review Board Statement: Not applicable.

Informed Consent Statement: Not applicable.

Data Availability Statement: The data presented in this study are available upon request from the corresponding author.

Acknowledgments: We also thank the core facilities in the Faculty of Health Sciences—especially the drug development core, bioimaging, and stem cell core—for their excellent services.

Conflicts of Interest: The authors declare no conflict of interest.

References

1. Meng, Z.; Jiang, C.; Li, X.; Zhai, J. Calcein-modified multinanochannels on PET films for calcium-responsive nanogating. *ACS Appl. Mater. Interfaces* **2014**, *6*, 3794–3798. [[CrossRef](#)]
2. Niu, B.; Xiao, K.; Huang, X.; Zhang, Z.; Kong, X.Y.; Wang, Z.; Wen, L.; Jiang, L. High-Sensitivity Detection of Iron(III) by Dopamine-Modified Funnel-Shaped Nanochannels. *ACS Appl. Mater. Interfaces* **2018**, *10*, 22632–22639. [[CrossRef](#)]
3. Sun, Y.; Chen, S.; Chen, X.; Xu, Y.; Zhang, S.; Ouyang, Q.; Yang, G.; Li, H. A highly selective and recyclable NO-responsive nanochannel based on a spiroring opening-closing reaction strategy. *Nat. Commun.* **2019**, *10*, 1323. [[CrossRef](#)]

4. Xu, Y.; Sui, X.; Jiang, J.; Zhai, J.; Gao, L. Smooth Muscle Cell-Mimetic CO-Regulated Ion Nanochannels. *Adv. Mater.* **2016**, *28*, 10780–10785. [[CrossRef](#)]
5. Zhao, X.P.; Zhou, Y.; Zhang, Q.W.; Yang, D.R.; Wang, C.; Xia, X.H. Nanochannel-Ion Channel Hybrid Device for Ultrasensitive Monitoring of Biomolecular Recognition Events. *Anal. Chem.* **2019**, *91*, 1185–1193. [[CrossRef](#)]
6. Freedman, K.J.; Otto, L.M.; Ivanov, A.P.; Barik, A.; Oh, S.H.; Ediel, J.B. Nanopore sensing at ultra-low concentrations using single-molecule dielectrophoretic trapping. *Nat. Commun.* **2016**, *7*, 10217. [[CrossRef](#)]
7. Kong, Y.; Fan, X.; Zhang, M.; Hou, X.; Liu, Z.; Zhai, J.; Jiang, L. Nanofluidic diode based on branched alumina nanochannels with tunable ionic rectification. *ACS Appl. Mater. Interfaces* **2013**, *5*, 7931–7936. [[CrossRef](#)]
8. Zhang, D.; Zhou, S.; Liu, Y.; Fan, X.; Zhang, M.; Zhai, J.; Jiang, L. Self-Assembled Porphyrin Nanofiber Membrane-Decorated Alumina Channels for Enhanced Photoelectric Response. *ACS Nano* **2018**, *12*, 11169–11177. [[CrossRef](#)]
9. Xiao, K.; Chen, L.; Xie, G.; Li, P.; Kong, X.Y.; Wen, L.; Jiang, L. A bio-inspired dumbbell-shaped nanochannel with a controllable structure and ionic rectification. *Nanoscale* **2018**, *10*, 6850–6854. [[CrossRef](#)]
10. Zhang, H.; Tian, Y.; Hou, J.; Hou, X.; Hou, G.; Ou, R.; Wang, H.; Jiang, L. Bioinspired Smart Gate-Location-Controllable Single Nanochannels: Experiment and Theoretical Simulation. *ACS Nano* **2015**, *9*, 12264–12273. [[CrossRef](#)]
11. Gao, P.; Ma, Q.; Ding, D.; Wang, D.; Lou, X.; Zhai, T.; Xia, F. Distinct functional elements for outer-surface anti-interference and inner-wall ion gating of nanochannels. *Nat. Commun.* **2018**, *9*, 4557. [[CrossRef](#)]
12. Fang, R.; Zhang, H.; Yang, L.; Wang, H.; Tian, Y.; Zhang, X.; Jiang, L. Supramolecular Self-Assembly Induced Adjustable Multiple Gating States of Nanofluidic Diodes. *J. Am. Chem. Soc.* **2016**, *138*, 16372–16379. [[CrossRef](#)]
13. Wu, K.; Kong, X.Y.; Xiao, K.; Wei, Y.; Zhu, C.; Zhou, R.; Si, M.; Wang, J.; Zhang, Y.; Wen, L. Engineered Smart Gating Nanochannels for High Performance in Formaldehyde Detection and Removal. *Adv. Funct. Mater.* **2019**, *29*, 1807953. [[CrossRef](#)]
14. Guo, W.; Hong, F.; Liu, N.; Huang, J.; Wang, B.; Duan, R.; Lou, X.; Xia, F. Target-specific 3D DNA gatekeepers for biomimetic nanopores. *Adv. Mater.* **2015**, *27*, 2090–2095. [[CrossRef](#)]
15. Wang, C.; Zhao, X.P.; Liu, F.F.; Chen, Y.; Xia, X.H.; Li, J. Dendrimer-Au Nanoparticle Network Covered Alumina Membrane for Ion Rectification and Enhanced Bioanalysis. *Nano Lett.* **2020**, *20*, 1846–1854. [[CrossRef](#)]
16. Xu, Y.; Sui, X.; Guan, S.; Zhai, J.; Gao, L. Olfactory sensory neuron-mimetic CO₂ activated nanofluidic diode with fast response rate. *Adv. Mater.* **2015**, *27*, 1851–1855. [[CrossRef](#)]
17. Xie, G.; Xiao, K.; Zhang, Z.; Kong, X.Y.; Liu, Q.; Li, P.; Wen, L.; Jiang, L. A Bioinspired Switchable and Tunable Carbonate-Activated Nanofluidic Diode Based on a Single Nanochannel. *Angew. Chem. Int. Ed. Engl.* **2015**, *54*, 13664–13668. [[CrossRef](#)]
18. Perez-Mitta, G.; Peinetti, A.S.; Cortez, M.L.; Toimil-Molares, M.E.; Trautmann, C.; Azzaroni, O. Highly Sensitive Biosensing with Solid-State Nanopores Displaying Enzymatically Reconfigurable Rectification Properties. *Nano Lett.* **2018**, *18*, 3303–3310. [[CrossRef](#)]
19. Lu, L.; Zhou, L.; Chen, J.; Yan, F.; Liu, J.; Dong, X.; Xi, F.; Chen, P. Nanochannel-Confined Graphene Quantum Dots for Ultrasensitive Electrochemical Analysis of Complex Samples. *ACS Nano* **2018**, *12*, 12673–12681. [[CrossRef](#)]
20. Liu, J.; Fu, B.; Zhang, Z. Ionic Current Rectification Triggered Photoelectrochemical Chiral Sensing Platform for Recognition of Amino Acid Enantiomers on Self-Standing Nanochannel Arrays. *Anal. Chem.* **2020**, *92*, 8670–8674. [[CrossRef](#)]
21. Zhang, Q.; Liu, S.; Du, C.; Fu, Y.; Xiao, K.; Zhang, X.; Chen, J. Highly Selective and Sensitive microRNA-210 Assay Based on Dual-Signaling Electrochemical and Photocurrent-Polarity-Switching Strategies. *Anal. Chem.* **2021**, *93*, 14272–14279. [[CrossRef](#)]
22. Xu, X.; Hou, R.; Gao, P.; Miao, M.; Lou, X.; Liu, B.; Xia, F. Highly Robust Nanopore-Based Dual-Signal-Output Ion Detection System for Achieving Three Successive Calibration Curves. *Anal. Chem.* **2016**, *88*, 2386–2391. [[CrossRef](#)]
23. Xu, X.; Zhao, W.; Gao, P.; Li, H.; Feng, G.; Zhao, Z.; Lou, X. Coordination of the electrical and optical signals revealing nanochannels with an ‘onion-like’ gating mechanism and its sensing application. *NPG Asia Mater.* **2016**, *8*, e234. [[CrossRef](#)]
24. Hou, X.; Guo, W.; Xia, F.; Nie, F.Q.; Dong, H.; Tian, Y.; Wen, L.; Wang, L.; Cao, L.; Yang, Y.; et al. A Biomimetic Potassium Responsive Nanochannel: G-Quadruplex DNA Conformational Switching in a Synthetic Nanopore. *J. Am. Chem. Soc.* **2009**, *131*, 7800–7805. [[CrossRef](#)]
25. Tian, Y.; Zhang, Z.; Wen, L.; Ma, J.; Zhang, Y.; Liu, W.; Zhai, J.; Jiang, L. A biomimetic mercury(II)-gated single nanochannel. *Chem. Commun.* **2013**, *49*, 10679–10681. [[CrossRef](#)]
26. Shi, L.; Jia, F.; Wang, L.; Jalalah, M.; Al-Assiri, M.S.; Gao, T.; Harraz, F.A.; Li, G. Fabrication of an artificial ionic gate inspired by mercury-resistant bacteria for simple and sensitive detection of mercury ion. *Sens. Actuators B Chem.* **2021**, *326*, 128976. [[CrossRef](#)]
27. Nolan, E.M.; Lippard, S.J. Tools and Tactics for the Optical Detection of Mercuric Ion. *Chem. Rev.* **2008**, *108*, 3443–3480. [[CrossRef](#)]
28. Liu, T.; Dong, J.X.; Liu, S.G.; Li, N.; Lin, S.M.; Fan, Y.Z.; Lei, J.L.; Luo, H.Q.; Li, N.B. Carbon quantum dots prepared with polyethyleneimine as both reducing agent and stabilizer for synthesis of Ag/CQDs composite for Hg(2+) ions detection. *J. Hazard. Mater.* **2017**, *322*, 430–436. [[CrossRef](#)]
29. Monisha; Shrivastava, K.; Kant, T.; Patel, S.; Devi, R.; Dahariya, N.S.; Pervez, S.; Deb, M.K.; Rai, M.K.; Rai, J. Inkjet-printed paper-based colorimetric sensor coupled with smartphone for determination of mercury (Hg(2+)). *J. Hazard. Mater.* **2021**, *414*, 125440. [[CrossRef](#)]
30. Chaudhary, A.; Dwivedi, C.; Chawla, M.; Gupta, A.; Nandi, C.K. Lysine and dithiothreitol promoted ultrasensitive optical and colorimetric detection of mercury using anisotropic gold nanoparticles. *J. Mater. Chem. C* **2015**, *3*, 6962–6965. [[CrossRef](#)]
31. Chen, G.H.; Chen, W.Y.; Yen, Y.C.; Wang, C.W.; Chang, H.T.; Chen, C.F. Detection of mercury(II) ions using colorimetric gold nanoparticles on paper-based analytical devices. *Anal. Chem.* **2014**, *86*, 6843–6849. [[CrossRef](#)]

32. Kempahanumakkagari, S.; Malingappa, P.; Ambikapathi, G.; Kuramkote Shivanna, D. 2,7-Dichlorofluorescein Hydrazide as a New Fluorescent Probe for Mercury Quantification: Application to Industrial Effluents and Polluted Water Samples. *J. Spectrosc.* **2013**, *2013*, 276981. [[CrossRef](#)]
33. Satsoura, D.; Leber, B.; Andrews, D.W.; Fradin, C. Circumvention of fluorophore photobleaching in fluorescence fluctuation experiments: A beam scanning approach. *Chemphyschem* **2007**, *8*, 834–848. [[CrossRef](#)]
34. Gao, X.; Gao, Y.; Qi, R.; Han, L. One-pot synthesis of a recyclable ratiometric fluorescent probe based on MOFs for turn-on sensing of Mg^{2+} ions and bioimaging in live cells. *New J. Chem.* **2019**, *43*, 18377–18383. [[CrossRef](#)]
35. Wang, H.; Hou, S.; Wang, Q.; Wang, Z.; Fan, X.; Zhai, J. Dual-response for $Hg(2+)$ and $Ag(+)$ ions based on biomimetic funnel-shaped alumina nanochannels. *J. Mater. Chem. B* **2015**, *3*, 1699–1705. [[CrossRef](#)]
36. Mo, R.; Yuan, Q.; Yan, X.; Su, T.; Feng, Y.; Lv, L.; Zhou, C.; Hong, P.; Sun, S.; Li, C. A Mercury Ion Electrochemical Sensor Based on Porous Anodized Alumina Membrane Nanochannels Modified with DNA. *J. Electrochem. Soc.* **2018**, *165*, H750–H755. [[CrossRef](#)]
37. Xu, S.; Chen, L.; Li, J.; Guan, Y.; Lu, H. Novel Hg^{2+} -imprinted polymers based on thymine- Hg^{2+} -thymine interaction for highly selective preconcentration of Hg^{2+} in water samples. *J. Hazard. Mater.* **2012**, *237–238*, 347–354. [[CrossRef](#)]
38. Liu, Y.; Kong, Y.; Fan, X.; Zhai, J.; Jiang, L. N_3/Al_2O_3 composite nanochannels: Photoelectric and photoelectric-and-pH cooperatively controlled ion gating. *J. Mater. Chem. A* **2017**, *5*, 19220–19226. [[CrossRef](#)]
39. Zhang, D.; Ren, Y.; Fan, X.; Zhai, J.; Jiang, L. Photoassisted salt-concentration-biased electricity generation using cation-selective porphyrin-based nanochannels membrane. *Nano Energy* **2020**, *76*, 105086. [[CrossRef](#)]
40. Zhang, D.; Wang, Q.; Fan, X.; Zhang, M.; Zhai, J.; Jiang, L. An Effective Dark-Vis-UV Ternary Biomimetic Switching Based on N_3 /Spiropyran-Modified Nanochannels. *Adv. Mater.* **2018**, *30*, e1804862. [[CrossRef](#)]
41. Wang, Z.; Wu, D.; Wu, G.; Yang, N.; Wu, A. Modifying Fe_3O_4 microspheres with rhodamine hydrazide for selective detection and removal of Hg^{2+} ion in water. *J. Hazard. Mater.* **2013**, *244–245*, 621–627. [[CrossRef](#)]
42. Fechler, N.; Fellinger, T.-P.; Antonietti, M. One-pot synthesis of nitrogen–sulfur-co-doped carbons with tunable composition using a simple isothiocyanate ionic liquid. *J. Mater. Chem. A* **2013**, *1*, 14097–14102. [[CrossRef](#)]
43. Sui, X.; Zhang, Z.; Zhang, Z.; Wang, Z.; Li, C.; Yuan, H.; Gao, L.; Wen, L.; Fan, X.; Yang, L.; et al. Biomimetic Nanofluidic Diode Composed of Dual Amphoteric Channels Maintains Rectification Direction over a Wide pH Range. *Angew. Chem. Int. Ed. Engl.* **2016**, *55*, 13056–13060. [[CrossRef](#)] [[PubMed](#)]
44. Li, Y.; Tu, L.; Ma, X.; Chen, H.; Fan, Y.; Zhou, Q.; Sun, Y. Engineering a Smart Nanofluidic Sensor for High-Performance Peroxynitrite Sensing through a Spirocyclic Ring Open/Close Reaction Strategy. *ACS Sens.* **2021**, *6*, 808–814. [[CrossRef](#)]
45. Pandurangappa, M.; Kumar, K.S. Micellar mediated trace level quantification through the ring opening process. *Anal. Methods* **2011**, *3*, 715–723. [[CrossRef](#)] [[PubMed](#)]
46. Li, D.; Li, C.Y.; Li, Y.F.; Li, Z.; Xu, F. Rhodamine-based chemodosimeter for fluorescent determination of $Hg(2+)$ in 100% aqueous solution and in living cells. *Anal. Chim. Acta* **2016**, *934*, 218–225. [[CrossRef](#)] [[PubMed](#)]
47. Credi, A.; Balzani, V.; Langford, S.J.; Stoddart, J.F. Logic Operations at the Molecular Level. An XOR Gate Based on a Molecular Machine. *J. Am. Chem. Soc.* **1997**, *119*, 2679–2681. [[CrossRef](#)]
48. Privman, I.; Zhou, J.; Halánek, J.; Katz, E. Realization and Properties of Biochemical-Computing Biocatalytic XOR Gate Based on Signal Change. *J. Phys. Chem. B* **2010**, *114*, 13601–13608. [[CrossRef](#)]
49. Glionna, C.; Kumar, V.; Le Saux, G.; Pramanik, B.; Wagner, N.; Cohen-Luria, R.; Ashkenasy, G.; Ashkenasy, N. Dynamic Surface Layer Coiled Coil Proteins Processing Analog-to-Digital Information. *J. Am. Chem. Soc.* **2021**, *143*, 17441–17451. [[CrossRef](#)]